

Structure and Infrastructure Engineering

Maintenance, Management, Life-Cycle Design and Performance

ISSN: 1573-2479 (Print) 1744-8980 (Online) Journal homepage: <https://www.tandfonline.com/loi/nsie20>

Evaluating long-duration blast loads on steel columns using computational fluid dynamics

Jack W. Denny & Simon K. Clubley

To cite this article: Jack W. Denny & Simon K. Clubley (2019): Evaluating long-duration blast loads on steel columns using computational fluid dynamics, Structure and Infrastructure Engineering, DOI: [10.1080/15732479.2019.1599966](https://doi.org/10.1080/15732479.2019.1599966)

To link to this article: <https://doi.org/10.1080/15732479.2019.1599966>



© 2019 Crown Owned Copyright.
Reproduced with the permission of the
Controller of Her Majesty's Stationery Office
and UK Ministry of Defense.



Published online: 05 Jul 2019.



Submit your article to this journal [↗](#)




Article views: 153



View Crossmark data [↗](#)

Evaluating long-duration blast loads on steel columns using computational fluid dynamics

Jack W. Denny^a  and Simon K. Clubley^b

^aFaculty of Engineering and Physical Sciences, University of Southampton, Southampton, UK; ^bSchool of Architecture, Building and Civil Engineering, Loughborough University, Loughborough, UK

ABSTRACT

Long-duration blasts are typically defined by positive pressure durations exceeding 100 ms. Such blasts can generate dynamic pressures (blast winds) capable of exerting damaging drag loads on comparatively slender structural components such as columns. With limited drag coefficient availability for specific structural geometries, Computational Fluid Dynamics (CFD) can be the only satisfactory approach for analysing blast loading on user-specified, finite geometries. The ability to analyse long-duration blasts with commercially available CFD programmes is still not confidently offered, with no prior studies examining the accuracy of modelling interaction with relatively much smaller, finite geometries. This paper presents a comparative investigation between numerical and experimental results to assess the predictive capacity of inviscid Eulerian CFD as a method for calculating long-duration blast drag loading on finite cross-sectional geometries. Full-scale long-duration blast experiments successfully measured surface pressure–time histories on a steel I-section column aligned at four orientations. Calculated pressure–time histories on exposed geometry surfaces demonstrated good agreement although reduced accuracy and under-prediction occurred on shielded surfaces manifesting as overestimated net loading. This study provides new understanding and awareness of the numerical capability and limitations of using CFD to calculate long-duration blast loads on intricate geometries.

ARTICLE HISTORY

Received 2 October 2018
Revised 20 December 2018
Accepted 10 February 2019

KEYWORDS

Long-duration; blast loading; multi-axis; Eulerian CFD; finite sections; computational fluid dynamics

1. Introduction

Long-duration blast waves are typically defined by positive pressure durations over 100 ms, developing in later stages of shock wave propagation i.e. in the ‘far field’ from the source of detonation (Denny & Clubley, 2019; Johns & Clubley, 2016). Blast waves reaching this later stage of propagation with sufficient energy to cause structural damage are characteristic of large-scale explosive events. In the modern world, these are commonly caused by hydrocarbon vapour cloud explosions at petrochemical facilities due to the nature in which volatile hydrocarbons are stored, equating to large amounts of potential energy. Notable recent examples include the 2005 ‘Buncefield Disaster’, exhibiting an estimated TNT equivalence of 105–250 T (Atkinson & Cusco, 2011; Steel Construction Institute, 2009). Other causes include the detonation of volatile industrial chemicals, particularly at processing and storage facilities. For example, the 2013 West Texas fertiliser plant explosion in which a fire caused the detonation of 30 T of ammonium nitrate caused a blast with an estimated 12.5 T TNT equivalence (U.S. Chemical Safety Board, 2013). The prevalence of such accidents highlights a growing need to be able to accurately model the loading and subsequent response of structures to long-duration blasts.

Long-duration blasts are extremely powerful, generating substantial impulse and non-trivial dynamic pressures.

Importantly, long pressure durations enable greater kinetic mobilisation of air particles behind the blast front, thereby generating dynamic pressures (blast winds) capable of exerting significant drag loads on slender structural elements such as columns. Structures and their constituent members can be subjected to blast waves from various angles of incidence depending on the location of detonation; this may arise in industrial operations where volatile, explosive materials are confined to certain areas of a facility.

Correctly characterising blast loading exerted on structural elements is essential for deriving reliable structural response solutions. When long-duration blasts interact with comparatively slender structural elements such as individual columns, the diffraction loading phase is reduced to a short-duration spike of reflected pressure as the blast envelops the column, followed by loading due to flow of the displaced air i.e. drag loading (Denny, 2017; Denny & Clubley, 2019). This is due to rapid equalisation of blast overpressures associated with the small section dimensions in comparison to blast wavelength (Denny, 2017; Denny & Clubley, 2019). Column elements are therefore ‘drag-sensitive’ where translational drag loading resulting from dynamic pressures has a predominant effect. Characterising time varying blast loads on respective surfaces of structural elements can be very complex, particularly when considering different angles of incidence. Drag loading is directly proportional to the



Figure 1. ABT, MOD Shoeburyness, UK (Clubley 2013).

dynamic pressure regime and influenced by the structural geometry and orientation. The density and viscosity of the air flowing around the section has a direct effect on the drag forces exerted in conjunction with complex aerodynamic and boundary layer effects such as flow separation and wake. Given inherent complexity, engineers opt to simplify and expedite the calculation of translational drag loading on a structure by employing drag coefficients, which approximate all these factors within a single modifier. In the majority of cases, drag coefficients are case dependent and determined experimentally. The concept of modifying the product of dynamic pressure and projected area by a dimensionless drag coefficient, C_D , has been universally adopted in blast design guidance and literature (Krauthammer, 2008; Mays & Smith, 1995; Smith & Hetherington, 1994; US Department of Defense (DoD), 2008). The resulting drag force, $F_X(t)$, exerted on a body with respect to time is related to the incident dynamic pressure $q(t)$, the projected area normal to the blast wind direction, A_X and the drag coefficient, C_D :

$$F_X(t) = C_D \cdot A_X \cdot q(t) \quad (1)$$

While there has been considerable prior research into characterising clearing and blast interaction with finite structures and columns (Ballantyne, Whittaker, Dargush, & Aref, 2010; Rigby et al., 2014; Shi, Hao, & Li, 2007), these studies concentrate on short-duration blasts for which drag loading is relatively inconsequential. As a result, the prevalence of blast drag coefficients in open literature is limited, particularly when considering specific finite geometries such as structural I-sections. Proposed drag coefficients in literature also demonstrate inconsistency and are typically single values lacking provision for different angles of incidence; therefore, it is simply unknown how to characterise drag loading for different orientations.

In such cases where simplified empirical methods are rendered unusable, Computational Fluid Dynamics (CFD) may be the only satisfactory approach available for calculating blast interaction and loading on user-specified geometries. CFD is a well-established numerical method utilising the physical equations of fluid dynamics to simulate the propagation of fluid flow through a domain and around objects. Blast waves are characterised by a pulse of compressed air travelling through a given medium and can

therefore be modelled using CFD. Fluid dynamics are the fundamental physical equations underpinning CFD and are based on the continuity, momentum and energy equations, collectively known as the Navier–Stokes equations (Anderson, 2009; Mays & Smith, 1995; Smith & Hetherington, 1994). A particular case exists when the fluid is assumed to be ‘inviscid’ (i.e. an ideal fluid, in which kinematic and dynamic viscosity, μ and ν are zero, and thus the fluid is incapable of developing shear stresses) and no heat conduction exists (Mays & Smith, 1995). Inviscid flows might arise where the Reynolds number, Re , is high (Craft, 2010). The governing equations for an unsteady, three-dimensional, compressible inviscid flow are obtained by dropping the viscous terms of the Navier–Stokes equations, giving rise to the Euler equations which represent the conservation of mass (continuity), momentum and energy (Equations 2–4) (Anderson, 2009):

Conservation of mass: (non-conservative form)

$$\frac{D\rho}{Dt} + \rho \nabla \cdot \vec{V} = 0 \quad (2)$$

Conservation of momentum: (non-conservative form)

$$\begin{aligned} \rho \frac{Du}{Dt} &= -\frac{\partial p}{\partial x} + \rho f_x \\ \rho \frac{Dv}{Dt} &= -\frac{\partial p}{\partial y} + \rho f_y \\ \rho \frac{Dw}{Dt} &= -\frac{\partial p}{\partial z} + \rho f_z \end{aligned} \quad (3)$$

Conservation of energy: (non-conservative form)

$$\rho \frac{D}{Dt} \left(e + \frac{V^2}{2} \right) = p\dot{q} - \frac{\partial(up)}{\partial x} - \frac{\partial(vp)}{\partial y} - \frac{\partial(wp)}{\partial z} + \rho \vec{f} \cdot \vec{V} \quad (4)$$

where ρ is the fluid density, V is the fluid velocity, p is the fluid pressure, e is the internal energy per unit mass of the fluid, \dot{q} is the rate of volumetric heat addition per unit mass, $f_{x,y,z}$ as the component body force per unit mass acting on the fluid element, D/Dt is the derivative with respect

Table 1. I-section column specimen properties.

Column section	UKC 203 × 203 × 46
Experimental concept	8 Endevco 8515C-50 surface-mounted pressure transducers measure multi-axis blast interaction
Steel grade	S275
Second moment of area (cm ⁴)	$I_{yy} = 4568$ $I_{zz} = 1548$
Column total height (cm)	300

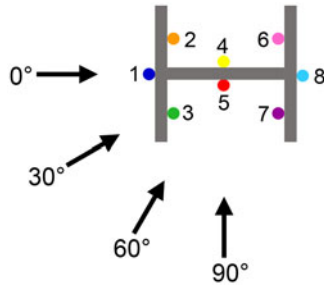


Figure 2. Multi-axis loading angle and surface pressure gauge numbering convention.



Figure 3. Cantilever I-section configuration in the ABT viewed upstream for the 30° I-section orientation.

to time and $\partial/\partial x$, $\partial/\partial y$ and $\partial/\partial z$ are the partial derivatives with respect to three-dimensional space.

At present, commercially available CFD programmes or 'hydrocodes' with shock wave modelling capabilities are based



Figure 4. (a) Circular base plate. (b) Endevco 8515C-50 surface pressure transducers.

on solving the inviscid Euler equations. Such inviscid flow assumptions are appropriate for high-speed external flows around streamlined bodies or 'free-stream' flows at sufficient distance from a body (Craft, 2010). Shock wave propagation in air is therefore considered an inviscid problem and solution of the Euler equations provides adequate approximation (Mays & Smith, 1995). Inviscid flows neglect viscous shear stresses and are often assumed irrotational (i.e. no vorticity), although such approximation and assumptions are not valid within boundary layers or wake regions (Craft, 2010). Schraml and Hisley (1995) investigated the accuracy of both inviscid Euler and full Navier–Stokes flow solvers to model short-duration blast interaction with a 2-D square target with comparison to experimental measurements performed inside a shock tube. Results of the study demonstrated that the inviscid solver was less accurate than the viscous (Navier–Stokes) flow solver at resolving pressure histories on the side surfaces of the square target during the drag phase (Schraml & Hisley, 1995).

While viscous Navier–Stokes solvers have potential to resolve complex aerodynamic effects pertaining to the drag phase, no such commercial codes that confidently offer shock wave modelling are openly available. Commercially available hydrocodes with blast modelling capabilities remain based on the inviscid Euler equations such as Air3D (Rose, 2006) and ANSYS Autodyn (Century Dynamics, 2011). With the majority of contemporary blast research concentrated on short-duration explosions where drag loading is inconsequential, such inviscid Euler solvers are adequate and have demonstrated

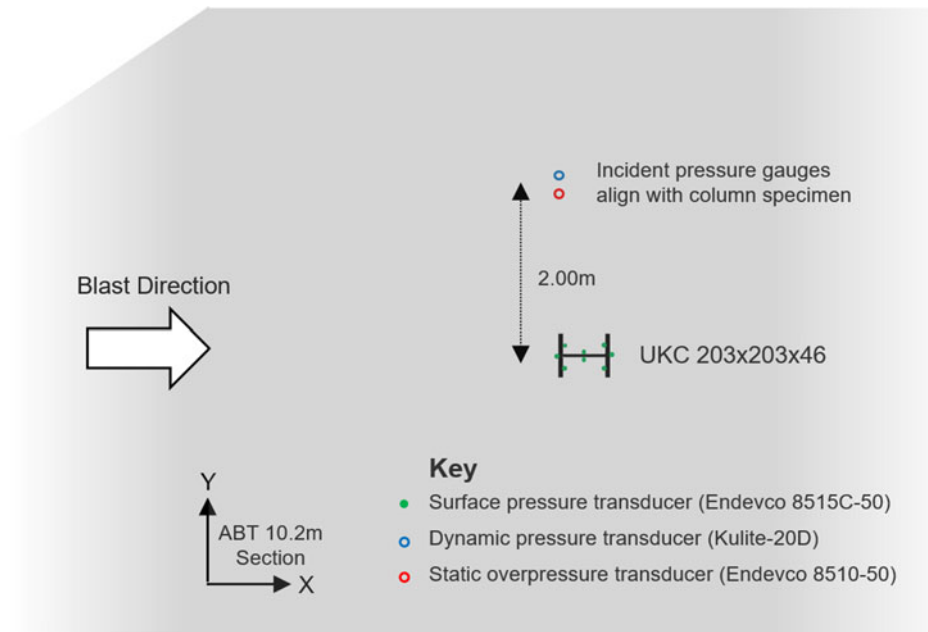


Figure 5. Plan view schematic of the trial configuration for the 0° I-section orientation.

satisfactory agreement in prior studies (Ballantyne, Whittaker, Aref, & Dargush, 2009; Ballantyne et al., 2010; Chapman, Rose, & Smith, 1995; Remennikov & Rose, 2005; Sherkar, Whittaker, & Aref, 2010). However, no prior studies have assessed the accuracy and reliability of Eulerian CFD for modelling long-duration blast interaction with small, intricate geometries where drag loading is non-trivial.

Modelling long-duration blasts with CFD is still not reliably offered. Such blasts inherently involve long positive pressure durations ($t^+ > 100$ ms), large wavelengths and standoff distances which readily give rise to unmanageable solution domains, impractical simulation times and extensive computational resource. The challenging spatial scale of the problem is exacerbated when attempting to model interaction with much smaller, intricate geometries that require high resolution mesh. In such cases, careful employment of a mesh-rezoning technique is essential to address the relative spatial scales and manage the associated computational expense.

This paper presents a comparative investigation between numerical simulations and experimental results to assess the capability of Eulerian CFD analysis to characterise long-duration blast drag loading on a relatively small I-section geometry from different angles of incidence. Blast loading on I-shape geometries presents a particularly challenging scenario, giving rise to complex blast interaction due to axis sensitivity and finite geometric features (web and flanges). In the absence of verified drag coefficients for I-sections or provision for multi-axis interaction, Eulerian CFD analysis is evaluated as a potential tool for calculating long-duration blast drag loading on finite geometries.

2. Experimental work

2.1. Experimental methodology

Constructed in 1964, the Air Blast Tunnel (ABT) is one of few facilities in the world capable of examining the

structural response to long-duration blast waves (Figure 1). At approximately 200 m long, the tunnel has two main test sections: a 4.9 m diameter and 10.2 m diameter. The ABT is capable of generating blast waves with long-duration characteristics; a peak overpressure of $p_i \approx 55$ kPa and positive phase duration of $t^+ \approx 155$ ms are attainable at maximum power in the 10.2 m section. A driver charge is located in a 1.8 m diameter section and the long increasing diameter of the tunnel effectively re-shapes the blast into a substantially longer wavelength with characteristics of a near-planar long-duration, Mach stem pulse. The exhaust of the tunnel is equipped with a rarefaction wave eliminator which assists in the reduction of unwanted reflections in the upstream direction (Figure 1). For each experiment, blast waves with consistent parameters were sought at maximum power inside the 10.2 m section. Through re-shaping the propagating shock wave, a blast is achieved with TNT equivalence of approximately 200 T at a 200 m stand-off distance when calculated via the Kingery and Bulmash predictive polynomial equations (Kingery & Bulmash, 1984).

Four long-duration blast trials were conducted using the ABT to investigate and quantify the influence of angle of incidence on resultant blast loading of a 3.00 m steel UKC $203 \times 203 \times 46$ I-section column (Table 1). Four angles of incidence were investigated by aligning the column at orientations of 0° , 30° , 60° and 90° to the experimental blast propagation inside the ABT (Figure 2). The column was fixed to the ground in a cantilever configuration and designed to respond with minimal elastic response, allowing repeat firings of the same section at different orientations (Figure 3). A bespoke adjustable base plate design provided a fully fixed support condition that allowed the section to be rotated in situ between trials to achieve the specified orientations (Figure 4). The I-section was instrumented with eight Endevco 8515C-50 pressure transducers secured to the centre point of each surface at mid-height to measure blast

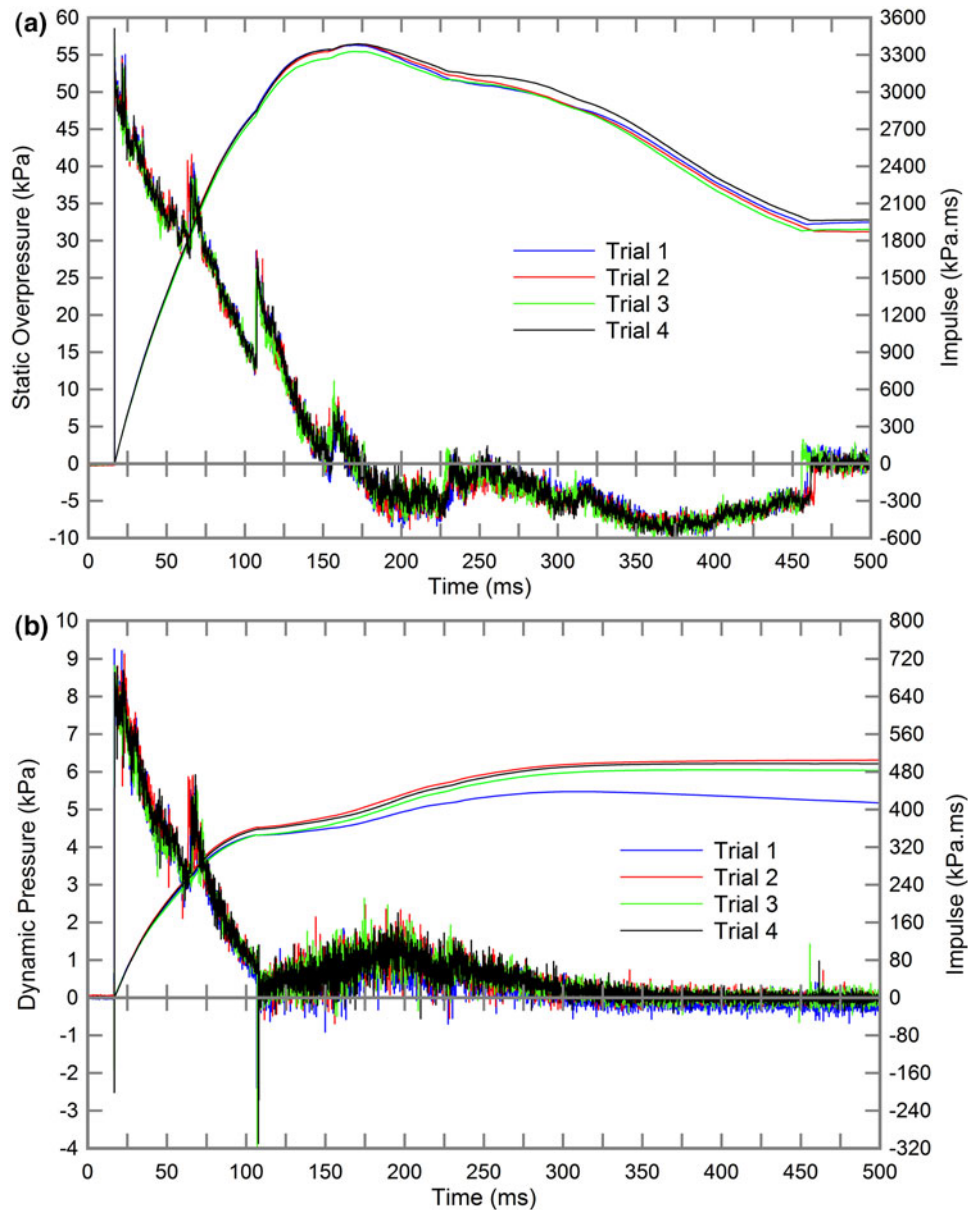


Figure 6. (a) Static overpressure-time history and cumulative impulse (Trials 1–4). (b) Dynamic overpressure-time history and cumulative impulse (Trials 1–4).

interaction and pressures exerted on respective column surfaces (Figures 2 and 4). The incident blast environment was measured using Endevco 8510-50 static overpressure gauges and Kulite-20D dynamic pressure gauges to record peak overpressures, specific impulse and positive phase durations for the free-field environment (Figure 5).

2.2. Incident blast environment

Static and dynamic pressure-time histories were measured inside the ABT at a location 2.00 m adjacent to the column section to assess the incident blast environment and trial repeatability. Recorded static and dynamic pressure-time histories were characteristic of a Friedlander exponential decay blast wave although some non-ideal discontinuities were observed throughout the positive phase duration (Figure 6). This phenomena occurred for all four trials and can also be seen in archival pressure data for the ABT

Table 2. Incident blast environment—static overpressure parameters.

Incident blast overpressure parameters	Trial 1	Trial 2	Trial 3	Trial 4	Mean
Peak incident overpressure, p_i (kPa)	59.1	58.4	58.6	58.5	58.7
Positive phase duration, t^+ (ms)	154.2	154.8	152.6	155.6	154.3
Positive phase incident impulse, I_i (kPa.ms)	3377	3387	3327	3389	3370

operating at maximum power, indicating this pattern is characteristic of the ABT performance envelope (Clough, 2016; Clubleby, 2014).

Static overpressures recorded over the four trials demonstrated good agreement and successfully represented the design blast conditions. A mean peak incident static overpressure value of $p_i=58.7$ kPa was recorded across the four trials (Table 2). A mean positive phase duration of $t^+=154.3$ ms and mean positive phase total impulse of $I_i=3370$ kPa.ms were recorded respectively (Table 2).

Table 3. Incident blast wave variation through trials 1–4.

		Mean values (\bar{X})			Standard deviation (σ)					
Trials	Gauge	p_i (kPa)	t^+ (ms)	I_i (kPa.ms)	p_i (kPa)	t^+ (ms)	I_i (kPa.ms)	p_i (% of \bar{X})	t^+ (% of \bar{X})	I_i (% of \bar{X})
(a) Static overpressure										
1–4	PI(L)	58.7	154.3	3370	0.3	1.093	25.3	0.46%	0.71%	0.75%
		Mean values (\bar{X})			Standard deviation (σ)					
Trials	Gauge	q (kPa)	t_q^+ (ms)	I_q (kPa ms)	q (kPa)	t_q^+ (ms)	I_q (kPa ms)	q (% of \bar{X})	t_q^+ (% of \bar{X})	I_q (% of \bar{X})
(b) Dynamic pressure										
1-4	PD(L)	9.0	317.1	463	0.1	22.2	19.7	0.92%	7.00%	4.26%

Table 4. Incident blast environment—dynamic pressure parameters.

Incident dynamic pressure parameters	Trial 1	Trial 2	Trial 3	Trial 4	Mean
Peak dynamic pressure, q (kPa)	9.1	9.0	9.1	8.9	9.0
Positive phase duration, t_q^+ (ms)	286.1	337.2	305.9	339.0	317.1.0
Positive phase dynamic impulse, I_q (kPa.ms)	438	484	450	480	463

Standard deviations for incident static overpressure and total impulse were small across the four trials with values representing only 0.46% and 0.75% of the mean, respectively, indicating a blast environment with good repeatability (Table 3a).

Peak dynamic pressures demonstrated good consistency with a mean value of 9.0 kPa (Table 4) and a small standard deviation representing 0.92% of the mean over the four trials (Table 3b). A mean dynamic impulse of $I_q=463$ kPa.ms was calculated with a standard deviation equivalent to 4.26% of the mean (Table 3b). This shows that a higher degree of variance occurred throughout the four trials, indicating dynamic pressures behind the shockwave are difficult to control under experimental conditions. Overall, the incident blast environment demonstrated good repeatability and it is acceptable to assume that the I-section column was subjected to effectively consistent incident blast conditions.

2.3. I-section blast interaction

For each I-section orientation examined, eight pressure transducers recorded pressure–time histories at the centre point of each surface of the UKC 203 × 203 × 46 I-section. Analysis of these pressure–time histories quantified respective surface impulses as a function of I-section orientation to the blast. Total impulses on each surface were calculated by integrating respective pressure–time histories over the positive phase duration and plotted as a function of I-section orientation in Figure 7 with incident total impulse overlaid for reference.

Surface impulses vary considerably with I-section orientation to the blast (Figure 7), influenced by both relative exposure of a particular surface to the blast and the presence of aerodynamic effects. Exposed surfaces exhibited the highest impulse; a maximum value was observed for the front flange (surface 1) at the 0° orientation and surfaces 3, 5 and 7 at the 90° orientation (Figure 7). Exposed surfaces measured total impulses exceeding the free-field incident impulse (Figure 7). For less exposed or ‘shielded’ surfaces, total impulses fall below the incident value (Figure 7). Surfaces 2, 4, 6 and 8 were comparably shielded throughout

orientations 0°–90° with total impulse values consistently below that of the incident blast wave (Figure 7). Collectively, these four shielded surfaces experienced minimum impulse at the 30° orientation (Figure 7), approximately 500 kPa.ms less than the free-field. This indicates a high degree of shielding where aerodynamic effects such as flow separation and turbulence manifest as reduced stagnation pressures on these surfaces.

At an orientation of 60°, the impulse exerted on the rear-facing flange (surface 8) continues to decrease to a minimum value while the shielded surfaces’ (2, 4 and 6) impulses gradually increase, indicating reduced shielding effects at this angle. At the 90° orientation, impulses for surfaces 2, 4 and 6 continue to increase to the order of 3210–3260 kPa.ms, comparable to an incident impulse (3389 kPa.ms). These relatively higher impulse values demonstrate that despite being shielded from the blast, reduced aerodynamic effects produce larger stagnation pressures loading rear surfaces. Analysis has demonstrated that surface impulses are greatly influenced by both relative exposure to the blast wave and the aerodynamic interaction with the section geometry features.

2.4. I-section net loading

Net force–time histories exerted on the entire column were calculated as a function of I-section orientation by multiplying respective surface pressure–time histories by their corresponding projected areas and resolved in the blast direction. As drag loading is predominant, pressures exerted on the column surfaces are resolved in the blast direction (consistent with the transient blast winds) for each orientation. Net force–time histories take account of respective I-section surface projected areas at each orientation and represent the resultant total loading with respect to time, $F_X(t)$ exerted on the column in the blast X-direction (Figure 8). Integrated net force–time histories with respect to time are overlaid, presenting the cumulative and total net impulse, I_X , exerted on the column as a function of orientation (Figure 8). Peak instantaneous forces on the column at each orientation exhibited similar values representing the rapid blast diffraction stage, although subsequent drag loading varied in magnitude (Figure 8). Higher transient drag loading was exerted on the column at orientations of 30° and 60° to the blast, as visible in the net force–time plots in Figure 8b, c. Total net impulse, I_X , accumulated over the positive phase duration is displayed as a function of section orientation in Figure 9. Similar net blast loading was exerted on the column at the

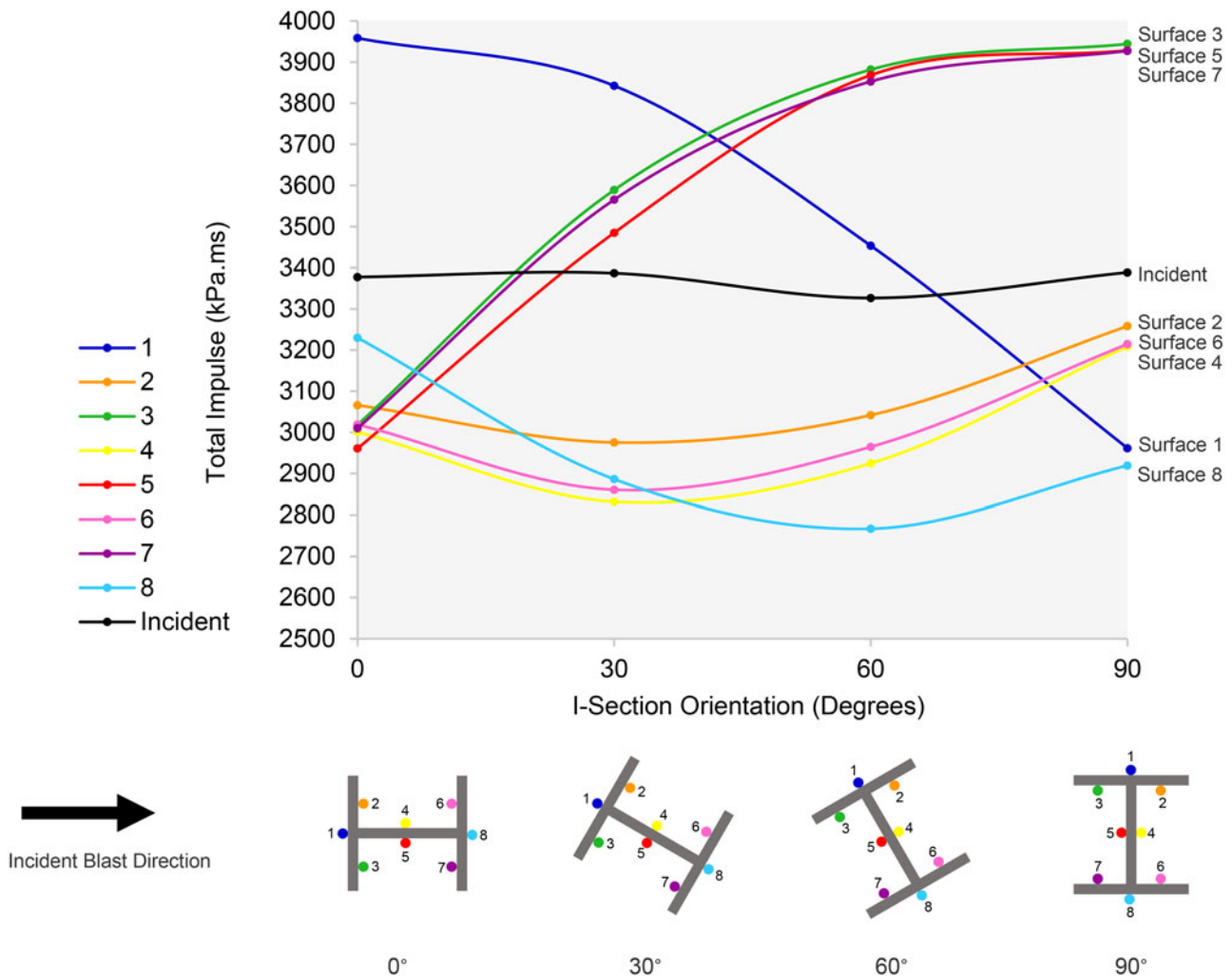


Figure 7. Surface total impulse variation with I-section orientation.

orthogonal 0° and 90° orientations with total impulses of 415 and 423 kN.ms, respectively (Figure 9).

Noticeably higher loading was exerted on the I-section at oblique orientations of 30° and 60°, demonstrated by higher total impulses, I_X (Figure 9). Maximum I-section loading occurred at the 60° orientation with a total impulse of $I_X=662$ kN.ms, 60% and 56% higher than the column orientated at 0° and 90° respectively (Figure 9). The second highest loading occurred at the 30° orientation with a total impulse of $I_X=567$ kN.ms, slightly less than the column orientated at 60°. The 30° column orientation resulted in 36% higher total net impulse than at 0° which can be attributed to the section's increased projected area to the blast, which also increased by 36%. The 60° orientation gave rise to higher loading than at 30° with a total impulse increase of 17% ($I_X=662$ kN.ms) and raised loading rates (steeper cumulative impulse gradient) despite the same projected area. By consideration of individual surface impulse, higher loading at the 60° orientation can be attributed to a lower restoring impulse on rear shielded surfaces at this orientation (Figure 7). Effectively, the geometry features at 60° causes the rear web (surface 4) to attain a much lower impulse than the exposed web (surface 5), thus generating relatively high net loading (Figure 7). The 60° I-section

orientation is therefore relatively more bluff than the other orientations, generating higher drag loading.

Overall, a non-symmetrical variation in total impulse with I-section orientation was observed, demonstrating that section aerodynamics are non-trivial and net loading on the column is not simply a function of projected area to the blast. These experimental results and analysis confirm that I-section orientation with respect to the blast has noticeable influence on net total loading exerted on a column.

3. Numerical modelling

3.1. Numerical methodology

Inviscid Eulerian CFD analyses were used to calculate surface pressure-time histories on respective I-section surfaces at the four axes corresponding to the experimental trials. ANSYS Autodyn (Century Dynamics, 2011) was utilised to perform CFD analyses primarily due to its domain 'rezoning' capabilities. Importantly, this managed computational expense by allowing a locally high-resolution mesh to be defined within a larger coarse mesh, suitable for representing the I-section geometry. Numerical modelling was performed in two main stages. Firstly, a one-dimensional

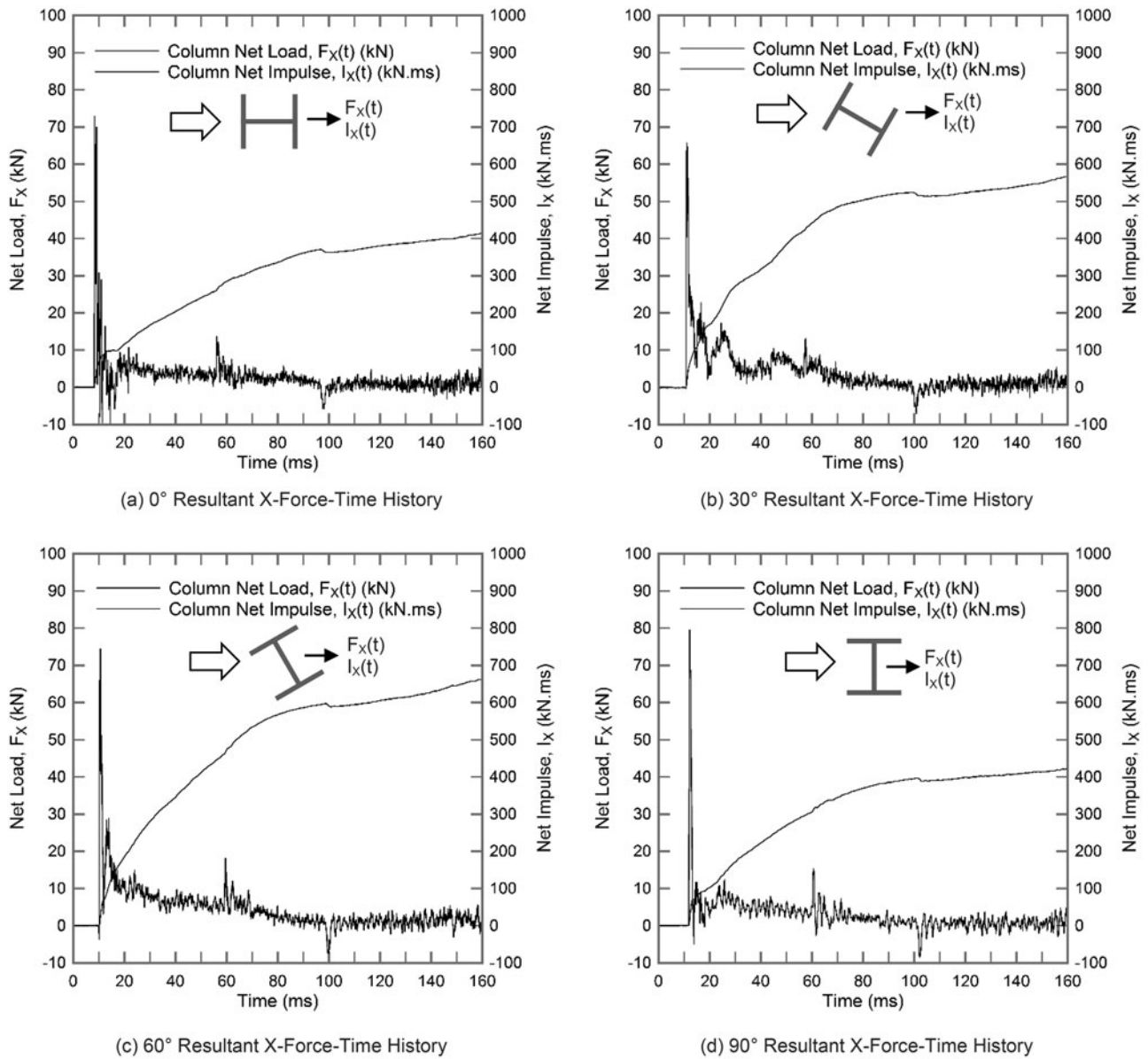


Figure 8. Net force–time histories and cumulative impulse exerted on I-section in blast X-direction. (a) 0° Resultant X-force–time history. (b) 30° Resultant X-force–time history. (c) 60° Resultant X-force–time history. (d) 90° Resultant X-force–time history.

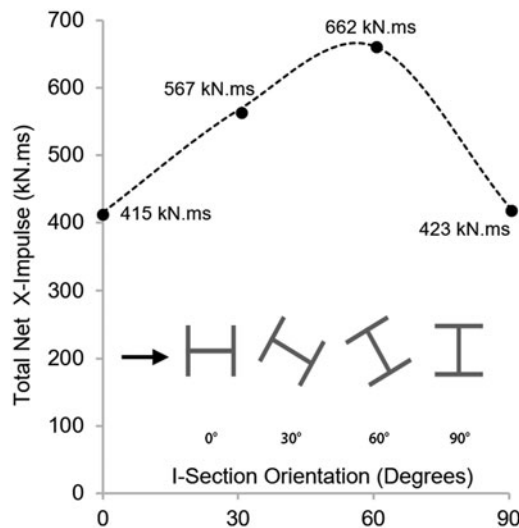


Figure 9. Calculated net total impulses exerted in X-direction on I-section at different orientations.

(1D) CFD analysis of a spherical free-air explosion to generate a long-duration blast wave with blast parameters equivalent to the experimental incident conditions. Secondly, two-dimensional (2D) inviscid Eulerian CFD analyses were integrated by ‘remapping’ the incident blast wave (from the prior 1D analysis) to propagate at specified angles across the domain to interact with an I-section geometry corresponding to the experiments. Surface pressure gauges assigned to the I-shape geometry measured pressure–time histories for comparison to experimental results.

One-dimensional (1D) CFD analysis of a spherical detonation of an explosive charge was performed to generate a numerical blast wave equivalent to the incident experimental blast conditions measured inside the ABT adjacent to the column. Long-duration blast characteristics inside the ABT were achieved by tunnel confinement of the propagating shock resulting from the detonation of a relatively small explosive charge. The incident experimental blast was

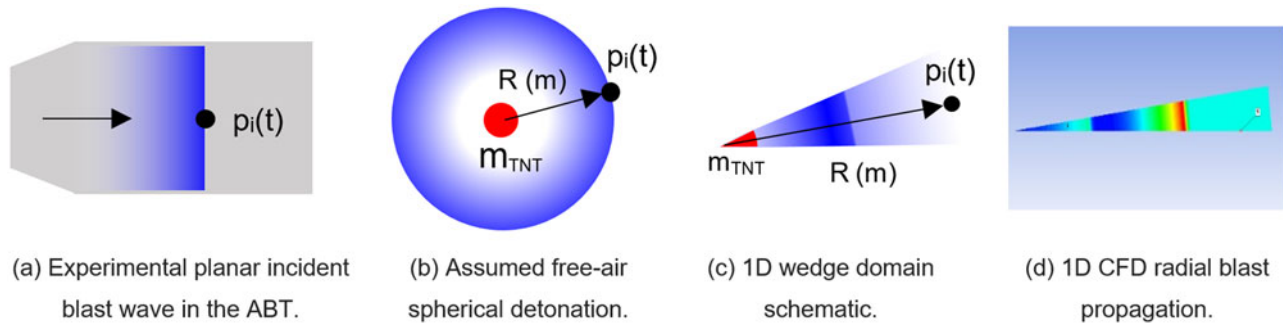


Figure 10. Modelling the ABT incident long-duration blast environment to the ABT assuming a spherical free-air detonation.

simulated numerically by modelling an assumed spherical free-air explosion of a certain explosive charge mass and standoff distance that generated equivalent blast wave parameters (Figure 10a, b).

Detonation of a spherical TNT charge and subsequent blast wave propagation in air was modelled using a radially symmetric one-dimensional (1D) wedge domain, representing radial shock propagation for an assumed spherical explosion. A sphere of TNT material was assigned at the apex of the wedge domain containing atmospheric air elements, such that the explosion and resulting shockwave propagate toward the open end (Figure 10c). The open end was assigned with an outflow boundary condition to allow air to exit after being accelerated by the shock wave. Explosive TNT material was modelled using the Jones–Wilkins–Lee (JWL) equation of state (Lee, Hornig, & Kury, 1968) and air was modelled as an ideal gas with an ambient pressure of 101.33 kPa by specifying an internal energy of 2.068×10^5 mJ/mm³. Initial temperature, density and adiabatic constant (specific heat ratio) γ of air cells were set to 288 °K (15 °C), 1.225 mg/cm³ and 1.4 respectively. The multi-material Euler–Godunov solver was used to model both the detonation of explosive material and subsequent shock wave propagation through air.

To replicate the experimental blast environment, a numerical blast wave with peak overpressure of $p_i \approx 58$ kPa, positive phase duration of $t^+ \approx 155$ ms and total impulse of $I_i \approx 3380$ kPa.ms was sought. Calculations based on the empirical work of Kingery and Bulmash (1984) were used to approximate the required TNT charge mass and standoff distance. Initial estimates suggested a detonation of 200 T TNT at a 200 m standoff, although this resulted in a numerical blast wave with underestimated total impulse and positive phase duration. Overestimation of incident total impulse using spreadsheets based on empirical blast parameters has similarly been noted in the works of Rigby et al. (2014). Bogosian, Ferritto, and Shi (2002) and Tabatabaei, Volz, Baird, Gliha, and Keener (2013) also found total incident impulses predicted using such empirical equations to be 15% and up to 40% higher respectively than found in experimental trials. This suggests that empirical spreadsheet tools are inherently conservative for incident impulse predictions, although they are still useful as an initial calibration tool.

The standoff distance and charge mass were subsequently raised to increase the positive phase duration and associated

impulse of the numerical blast wave. A pressure gauge was defined within the wedge domain at the specified standoff distance to monitor agreement with the experiments (Figure 10d). Using an iterative process, a charge mass of 268 T and standoff distance of 220 m was found to generate incident blast wave parameters consistent with those measured in the experimental ABT environment. CFD analysis was performed until the shock front propagated to the required standoff distance and then saved as a remap (.FIL) file to be utilised as initial conditions for subsequent 2D analyses.

Sensitivity studies were performed to assess the effect of mesh resolution (cell size) on the blast wave parameters measured at a standoff distance of 220 m from the detonation. Accuracy of the numerical blast wave was assessed in terms of agreement to the experimental blast incident overpressure, total incident impulse and positive phase duration. Different numbers of cells ranging from 250 to 30,000 cells (cell sizes ranging 8.3 to 1000 mm) were tested to investigate the influence on the resulting blast parameters. For comparison, dashed black lines in Figure 11a–c represent the respective values measured experimentally. Blast wave peak incident overpressure (Figure 11a), total impulse (Figure 11b) and positive phase duration (Figure 11c) were measured by the model gauge point and plotted against the total number of cells within the 1D wedge domain. A wedge domain comprising 25,000 10 mm cells was specified as it demonstrated convergence and good agreement to experimental incident blast parameters (Figure 11).

Two-dimensional (2D) CFD analyses were conducted to analyse blast interaction with the I-section geometry. This was an acceptable simplification as experimental pressure measurements on the I-section column were determined under near-planar blast conditions, thus uniform loading along the column height was assumed. Preliminary modelling identified that the planar domain had to accommodate the entire blast wavelength before and after the rigid cross-section. Transmissive ‘flow out’ boundary conditions were assigned to all sides to prevent reflection and ensure the interaction of a single, incident blast wave with the I-section geometry. These boundary conditions were not entirely efficient, with some localised reflection occurring at the domain sides. Dimensions of the 2D domain were therefore defined sufficiently large to prevent any boundary perturbations from interfering with regions of interest, particularly for the oblique axes blast propagation. Informed by sensitivity studies, the 2D domain was defined with dimensions of

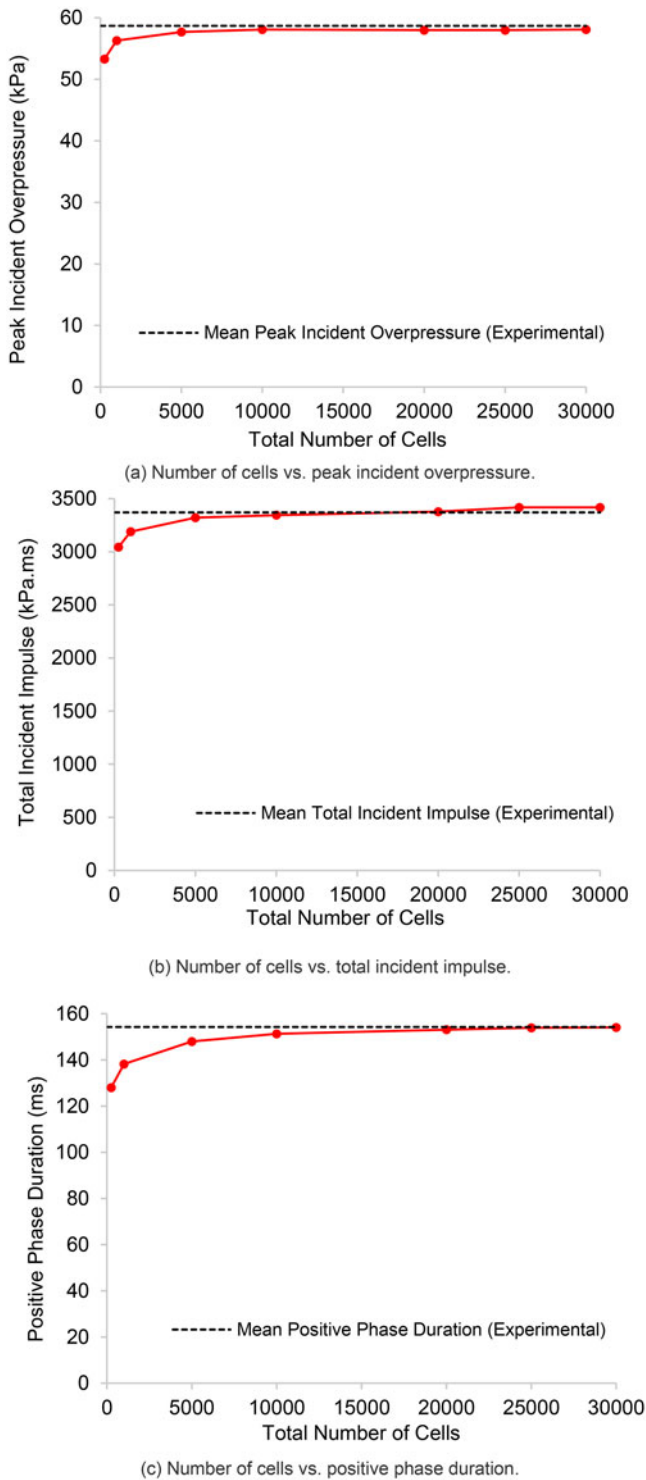


Figure 11. CFD mesh sensitivity study results.

200 m \times 200 m comprising 1 million cells to achieve maximum accuracy at manageable computational expense.

Utilising mesh rezoning, a 5 mm cell size was specified at the centre of the 2D domain to represent the I-section geometry (Figure 12). Exact representation of the UKC 203 \times 203 \times 46 geometry would require accuracy to the nearest tenth of a millimetre (0.1 mm) to fully define intricate features such as corner radii, resulting in unreasonable simulation times and computational demand. As a result, a 5 mm mesh resolution represented a compromise while

maintaining the correct geometry side lengths. The I-section geometry was defined using void cells within the domain to represent the I-section geometry tested in experimental trials (Figure 12). Reflective boundaries were assigned to void cells at geometric edges, thus defining a rigid I-section within the modelling domain. This is an acceptable assumption due to minimal elastic response observed in the experimental trials, therefore fluid–structure interaction effects were negligible. Pressure monitoring points were positioned in air cells adjacent to the centre point of each cross-sectional edge to record surface pressure–time histories, corresponding to experimental surface pressure transducers (Figure 12). Additional pressure monitoring points were specified 2.00 m from the column geometry to record the local incident free-field blast parameters consistent with the experimental setup.

Remap locations were positioned relative to the column geometry to create the desired angle of incidence, while maintaining the overall required stand-off distance (Figure 12). Coordinate positions of 1D remap locations relative to the column cross section were determined using trigonometric relations to satisfy the specified standoff distance and the angle of incidence for blast propagation across the planar domain. The square planar domain was defined and filled with air modelled as an ideal gas. A single material, Euler Flux Corrected Transport (FCT) solver was adopted as only the blast wave (air) itself required modelling. The Euler FCT solver has the advantage of being fast, efficient and specifically developed for blast applications (Börvik, Hanssen, Langseth, & Olovsson, 2009; Fairlie, 1998).

Blast waves from previous 1D analyses were remapped into the 2D domain and simulated for a duration of $t = 170$ ms allowing the blast to propagate and interact with the I-section geometry for the full positive phase duration. Pressure data were recorded at increments of 0.2 ms, sufficiently resolving overpressure histories while maintaining manageable data storage. Simulation run times varied for different orientations simulated, although typically required 46 CPU hours and ≈ 10 GB RAM.

3.2. Numerical modelling results & discussion

Numerical incident overpressure–time histories demonstrate good agreement with experimental data with respect to peak overpressure, positive phase duration and total impulse (Figure 13). Incident blast peak overpressure demonstrated reasonable agreement with experimental data, within 1.0% on average for the four experimental orientations modelled (Table 5a). Cumulative incident impulse calculated by the model also showed reasonable agreement to experimental trials, shown plotted in Figure 13. Total incident impulse calculated by the CFD models was slightly higher than experimental results with an average discrepancy of 1.4% across the four trials, representing a typical impulse error of ≈ 40 kPa.ms (Table 5b). Less agreement was observed for a 60° orientation equating to a total impulse discrepancy of 91.4 kPa.ms and percentage error of 2.7% (Table 5b). This was caused by a comparably lower incident impulse

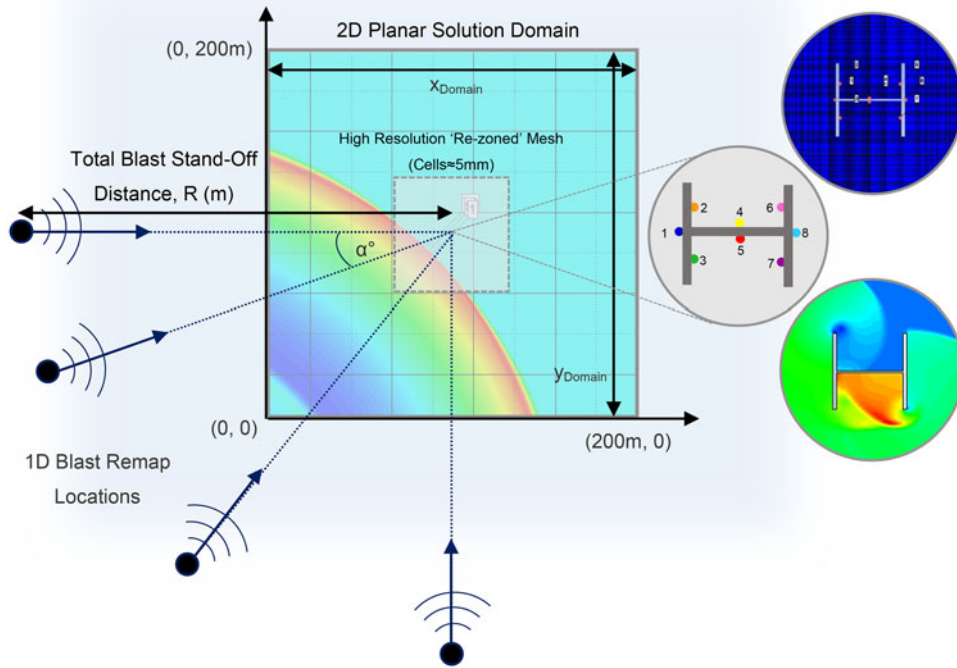


Figure 12. 2D domain setup and 1D remap locations to achieve multi-axis blast interaction.

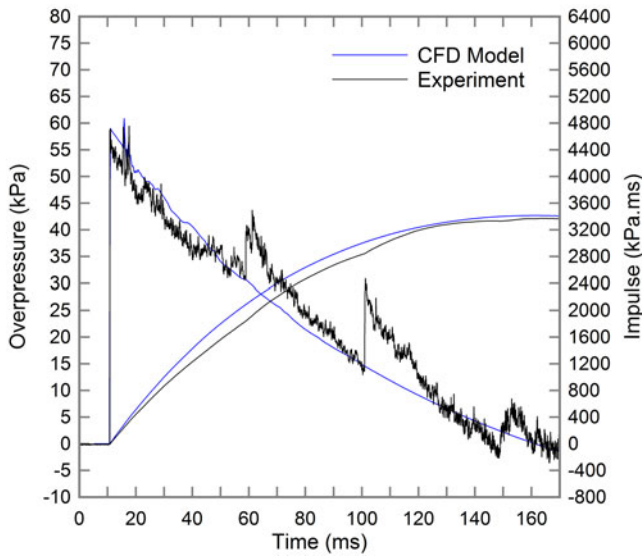


Figure 13. Incident overpressure-time histories and cumulative impulse: Experiment & CFD model.

measured in Trial 2, an example of minor experimental variance. Results from CFD show that a well-resolved incident blast wave consistent with the experiments was modelled.

Surface overpressure-time histories calculated by CFD models were integrated over the positive phase duration to calculate total surface impulse (Table 6, Figure 14). Despite a well-replicated incident blast wave, agreement between the CFD and experimental results varied considerably, depending on the surface and I-section orientation considered. Surface impulse discrepancies between CFD models and experimental results appear to correlate with surface

exposure to the blast. For the purpose of the analysis, 'exposed' or 'shielded' I-section surfaces are defined by total impulses either exceeding or below the incident value, shown in Figure 14a, b, respectively.

Total impulses on exposed surfaces 1, 3, 5 and 7 demonstrated comparably better agreement between the models and experimental results, particularly for orientations greater than 30° (Figure 14a). Analyses calculated surface total impulses with good agreement to experiments for surfaces 3, 5 and 7 across all orientations investigated, with mean absolute percentage errors of 3.5%, 1.8% and 2.8%, respectively (Table 6). As an example, pressure-time histories and cumulative impulse curves for surface 1 at the 60° I-section orientation displayed good agreement with the model, under-predicting experimental total impulse by 0.9% (Figure 15a and Table 6). Shielded surfaces, measuring total impulses less than incident, collectively demonstrated reduced agreement (Figure 14b). Total impulse discrepancies between the CFD model and experiments were generally larger for shielded surfaces 2, 4, 6 and 8, with mean absolute percentage errors of 5.9%, 5.2%, 5.6% and 12.8%, respectively, for the four orientations investigated (Figure 14b and Table 6). This suggests that Eulerian hydrocodes are less reliable at calculating pressure-time histories (and total impulse) on shielded surfaces for an intricate geometry.

The largest discrepancies between CFD models and experimental data consistently occurred at surface 8, with a mean absolute percentage error of 12.8% across four orientations (Figure 14b and Table 6). Models consistently calculated lower total impulse on surface 8 than measured in experiments by the order of 200–500 kPa.ms depending on orientation, representing percentage errors of 8.4%–17.5%

Table 5. Experimental and CFD model incident blast wave parameters.

(a) Peak incident blast overpressure.					
Peak Incident Overpressure, p_i (kPa)					
	0° (Trial 1)	30° (Trial 2)	60° (Trial 3)	90° (Trial 4)	Mean
Experiment	59.1	58.4	58.6	58.5	58.7
CFD Model	58.0	59.4	58.6	58.2	58.6
% Error	−1.9%	1.7%	0.0%	−0.5%	1.0%

(b) Total incident impulse.					
Incident Total Impulse, I_i (kPa.ms)					
	0° (Trial 1)	30° (Trial 2)	60° (Trial 3)	90° (Trial 4)	Mean
Experiment	3377	3387	3327	3389	3370
CFD Model	3418	3414	3418	3421	3418
% Error	1.2%	0.8%	2.7%	0.9%	1.4%

Table 6. Experimental and CFD model results: total impulse.

Total Impulse (kPa.ms)													
Pressure gauge location	0°			30°			60°			90°			Mean % Error (Surface)
	Experiment	CFD	Error	Experiment	CFD	Error	Experiment	CFD	Error	Experiment	CFD	Error	
Incident	3377	3418	1.2%	3387	3414	0.8%	3327	3418	2.7%	3389	3421	0.9%	1.4%
Surface 1	3958	3845	−2.9%	3842	3727	−3.0%	3454	3423	−0.9%	2961	2748	−7.2%	3.5%
Surface 2	3070	3153	2.7%	2975	2629	−11.7%	3042	2920	−4.0%	3258	3083	−5.4%	5.9%
Surface 3	3019	2803	−7.1%	3589	3452	−3.8%	3882	3837	−1.2%	3944	3875	−1.8%	3.5%
Surface 4	3001	3065	2.1%	2832	2478	−12.5%	2925	2844	−2.8%	3209	3095	−3.6%	5.2%
Surface 5	2961	2997	1.2%	3485	3340	−4.2%	3868	3845	−0.6%	3928	3881	−1.2%	1.8%
Surface 6	3019	3154	4.5%	2861	2481	−13.3%	2965	2934	−1.0%	3389	3421	0.9%	5.6%
Surface 7	3010	2793	−7.2%	3566	3466	−2.8%	3853	3853	0.0%	2961	2748	−7.2%	2.8%
Surface 8	3230	2873	−11.1%	2886	2382	−17.5%	2767	2368	−14.4%	3258	3083	−5.4%	12.8%
Mean % Error (across orientations)			4.5%			7.7%			3.1%			3.7%	

(Table 6). Reduced agreement occurred for surface 8 at the 30° orientation where models under-predicted total impulse by 496 kPa.ms (−17.5%). Overpressure–time histories and cumulative impulse curves calculated by models and corresponding experimental measurements for surface 8 at the 30° I-section orientation are shown in Figure 15b. While peak overpressure and positive phase durations show reasonable agreement, stagnation pressure histories beyond shockwave arrival results in relatively large cumulative and total impulse discrepancies (Figure 15b). Distorted, oscillating stagnation pressure profiles indicate the turbulent nature of the time-varying flow field in this location, characteristic of aerodynamic processes including shedding vortices, flow separation and low-pressure wake regions. The CFD model generally underestimated stagnation pressures, illustrated by diverging cumulative impulse curves beyond $t = 50$ ms in Figure 15b.

Discrepancies between the models and experimental measurements appear to be governed not only by shielding (relative surface exposure), but also the presence of time-varying aerodynamic processes. Surface 4 at the 90° I-section orientation for example, represents a fully shielded rear-facing surface where peak overpressure, positive phase duration and total impulses exhibit reasonable agreement between the model and experiments (Figure 15c). In this case, the model underestimated surface total impulse by 114.3 kPa.ms (−3.6%), representing a relatively small error by comparison (Table 6). Relatively better agreement for surface 4 at the 90° orientation in comparison to surface 8 at the oblique 30° orientation may therefore be attributed to reduced flow separation and wake. Such aerodynamic effects

are not well simulated in the model, symptomatic of the underpinning inviscid Euler solver.

Surface 6 presents further evidence that demonstrate the capability of Eulerian CFD to resolve stagnation pressure histories on shielded surfaces and the influence of aerodynamic processes. The model under-predicted total impulse by 380 kPa.ms (−13.3%) for surface 6 at the 30° orientation (Table 6). For this case, the model overpressure–time history exhibited an oscillating pressure profile generally below the measured experimental stagnation pressures, resulting in diverging cumulative impulse curves throughout the positive phase duration (Figure 15d). These results further indicate that inviscid Eulerian analysis cannot reliably simulate transient surface stagnation pressures beyond the initial arrival of the shock wave. Improved agreement was observed for the same surface at the 60° orientation, both in terms of stagnation pressure profiles and total impulse discrepancy (Table 6 and Figure 15e). Agreement for the 60° orientation underlines that aerodynamic processes such as flow separation, turbulence and low-pressure wake regions influence accuracy and reliability of the numerical model as both cases represent shielded scenarios. Without consideration of advanced aerodynamics, it is likely that flow separation originating at the top of the front flange at the 30° orientation shelters rear internal surfaces within a region of low-pressure wake that cannot be accurately simulated using an inviscid solver.

Analysis of model results has demonstrated that CFD can reliably simulate surface pressure histories on exposed surfaces of a finite cross-sectional geometry subjected to a long-duration blast. For surfaces directly exposed to blast, total impulse error between the numerical models and

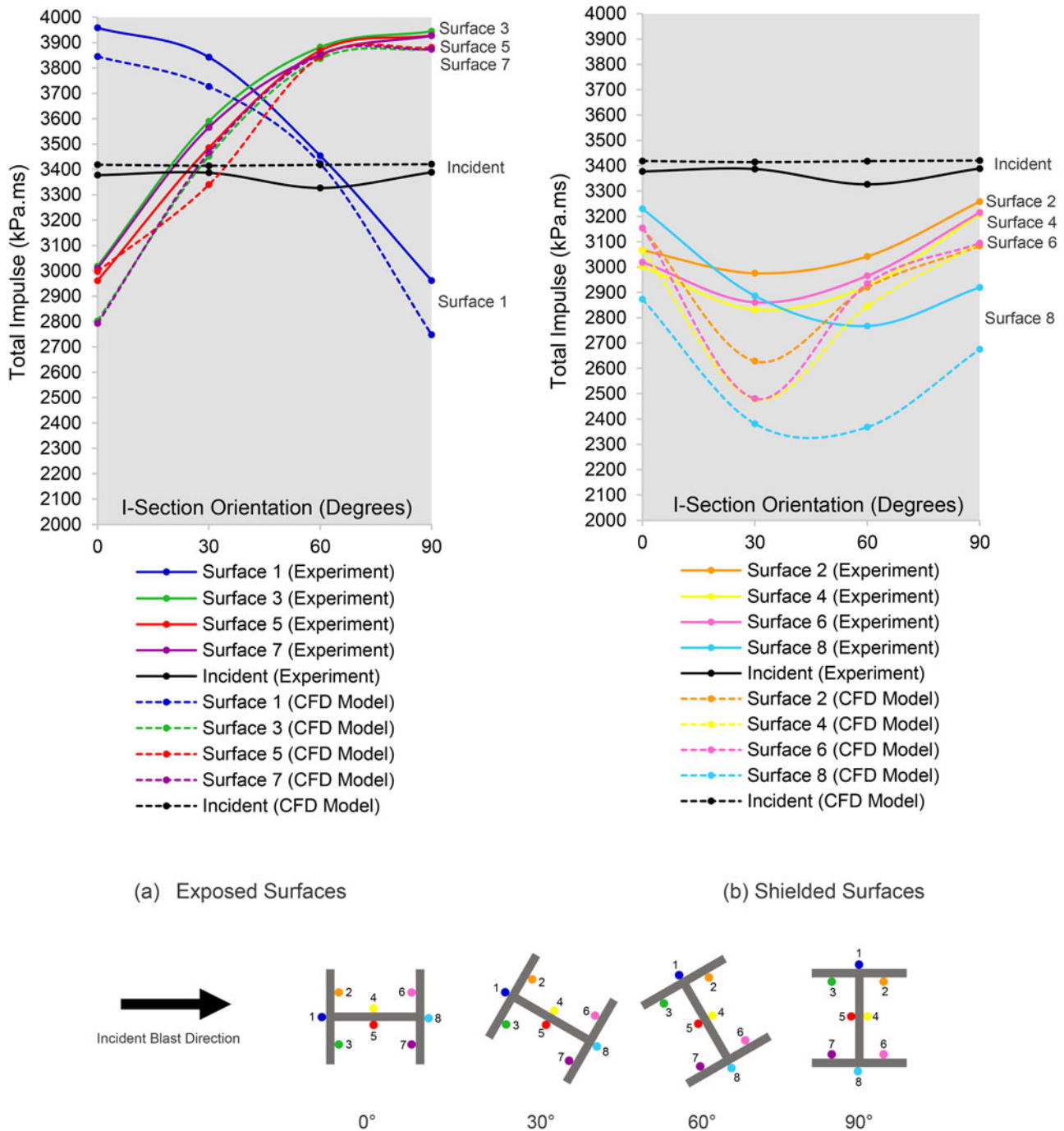


Figure 14. Surface total impulses measured experimentally and calculated by CFD models.

experiments was under 3.5% on average throughout all orientations investigated (Table 6). From analysis and comparison of experimental results, numerical discrepancies correlated with less-exposed, 'shielded' surfaces for the orientations investigated. With closer inspection of specific surfaces, larger discrepancies occurred in locations where flow separation, turbulence and wake regions give rise to significant influence. For these cases, models exhibited less accuracy due to incorrectly resolving complex aerodynamic flows, limited by the underpinning inviscid flow solver and absence of a turbulence model.

Surface pressure-time histories calculated by the hydrocode were multiplied by respective projected surface areas

and resolved in the blast X-direction to calculate net force-time plots and cumulative X-impulse exerted on the I-section geometry (Figure 16). Experimental net force-time plots and cumulative impulse curves are overlaid for comparison (Figure 16). Calculated net force-time histories visibly exceed those measured in experiments for I-section orientations of 30° and 60° (Figure 16b, c). Cumulative net impulse curves also exhibit steeper gradients for these orientations indicating that CFD analysis calculates a higher rate of net loading on the column geometry than measured in the experiments (Figure 16b, c). These cumulative impulse curves deviate from the experimental curves resulting in higher total impulse over the positive phase duration.

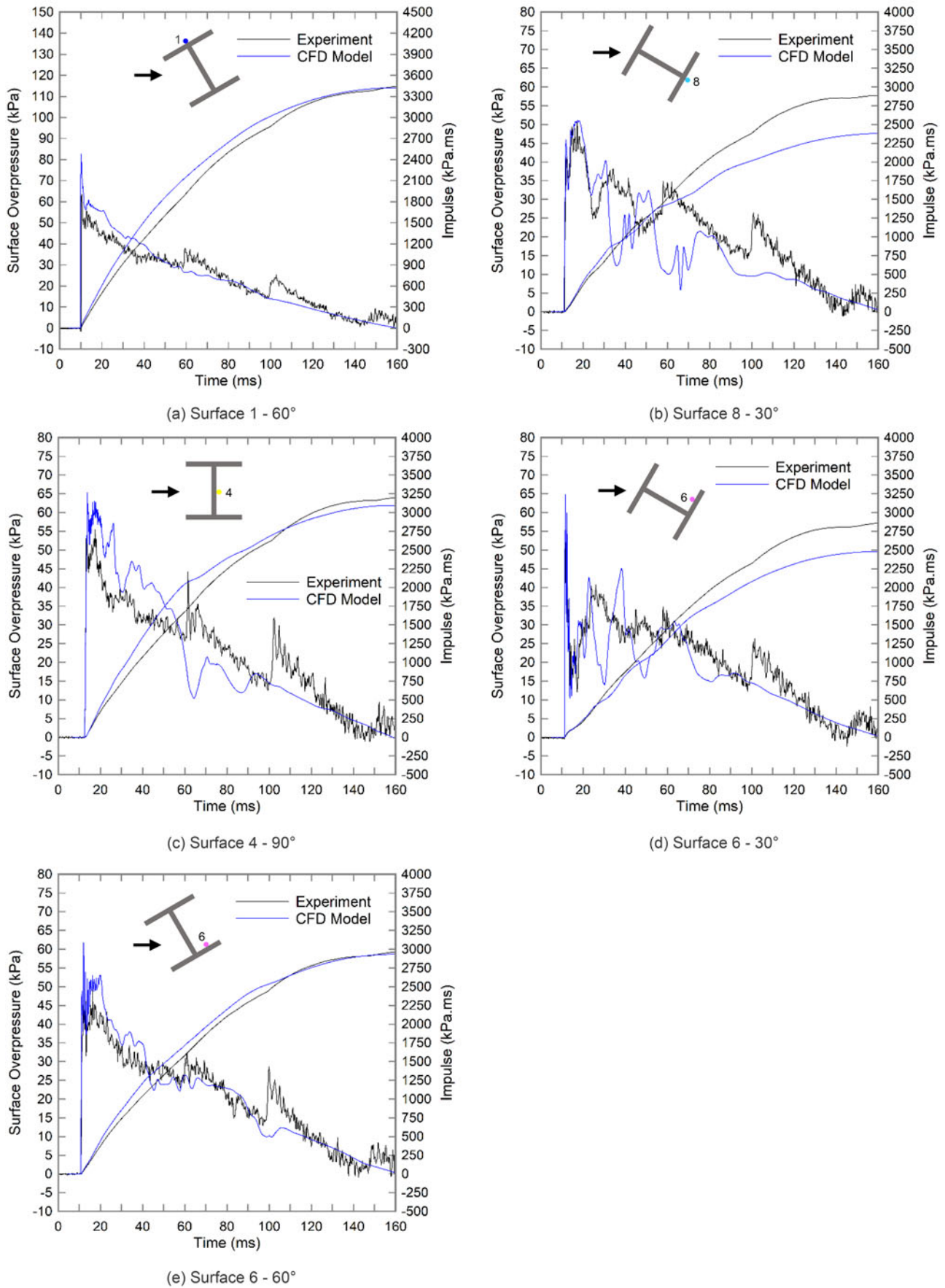


Figure 15. Comparative experimental and CFD model surface pressure-time histories. (a) Surface 1— 60° . (b) Surface 8— 30° . (c) Surface 4— 90° . (d) Surface 6— 30° . (e) Surface 6— 60° .

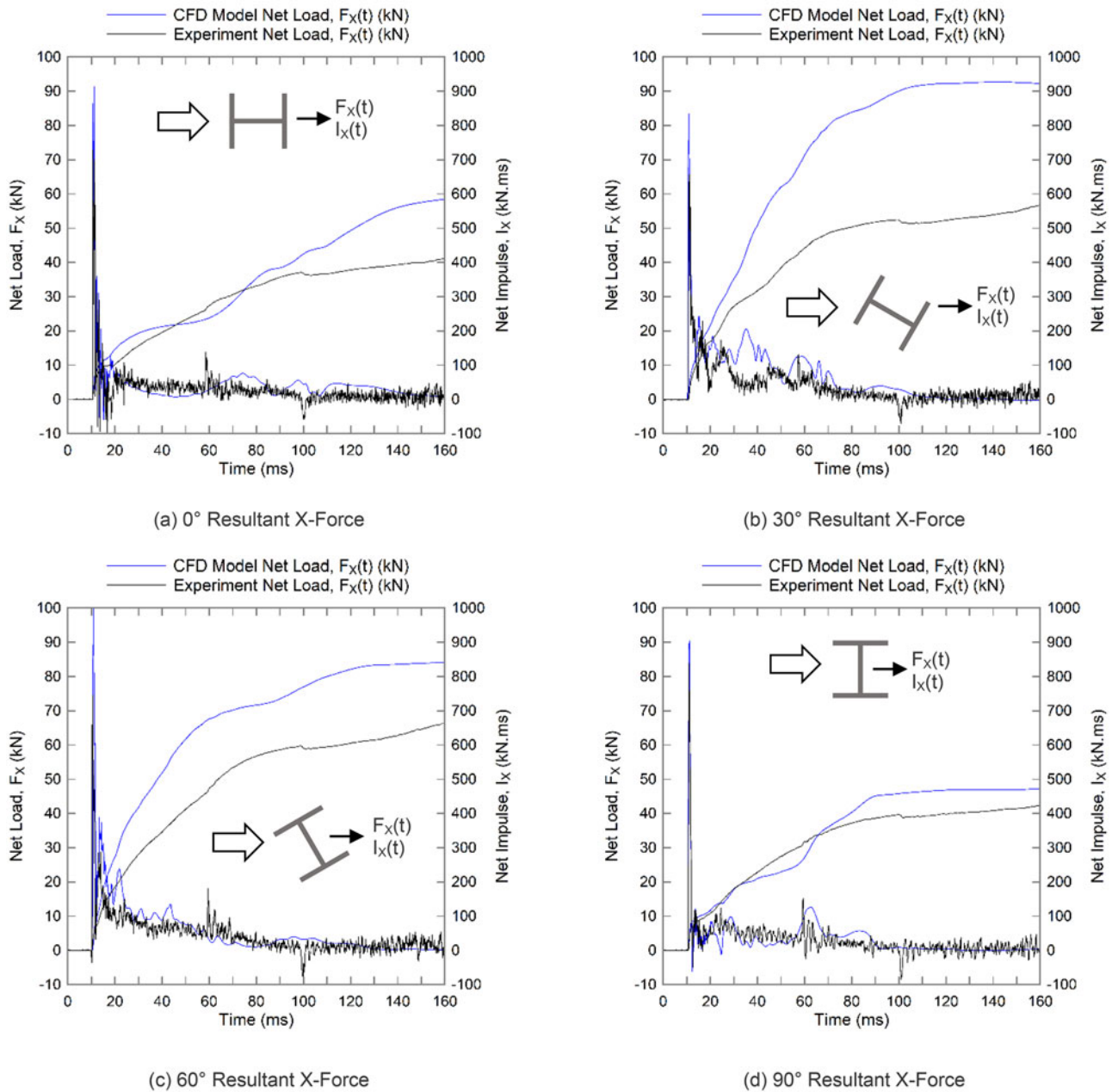


Figure 16. Net force-time histories and cumulative impulse: experimental results vs. CFD models. (a) 0° Resultant X-Force. (b) 30° Resultant X-Force. (c) 60° Resultant X-Force. (d) 90° Resultant X-Force.

Models of the orthogonal I-section orientations (0° and 90°) demonstrate comparably better agreement in terms of cumulative impulse curves although these also exhibited noticeable deviation from experimental results at a later time during the positive phase ($t > 100$ ms) (Figure 16a, d). This indicates that resultant loading exerted on I-sections aligned at 0° and 90° can be reasonably calculated using CFD analysis for approximately the first 100 ms of blast interaction.

Total net impulses accumulated over the positive phase duration ($t = t_a + 150$ ms) were plotted in Figure 17 and tabulated in Table 7. For all orientations, net total impulse calculated using CFD analysis exceed experimental results with large discrepancies except for the 90° orientation (Figure 17). At I-section orientations of 0° and 30°, net total

impulse calculated by analysis exceeded experimental values by 170 kN.ms (40.9%) and 356 kN.ms (62.3%), respectively (Table 7). Overall and importantly to note, hydrodynamic analyses over-predicted total and cumulative resultant impulse loading on the I-section geometry.

4. Conclusions

Inviscid Eulerian CFD modelling was performed to calculate blast loading exerted on a rigid I-section geometry at varied angles of incidence corresponding to four long-duration blast experiments. Localised mesh re-zoning and remapping techniques were employed to manage the challenging spatial scales pertaining to small intricate geometries and the large wavelengths inherent to long-duration blast problems.

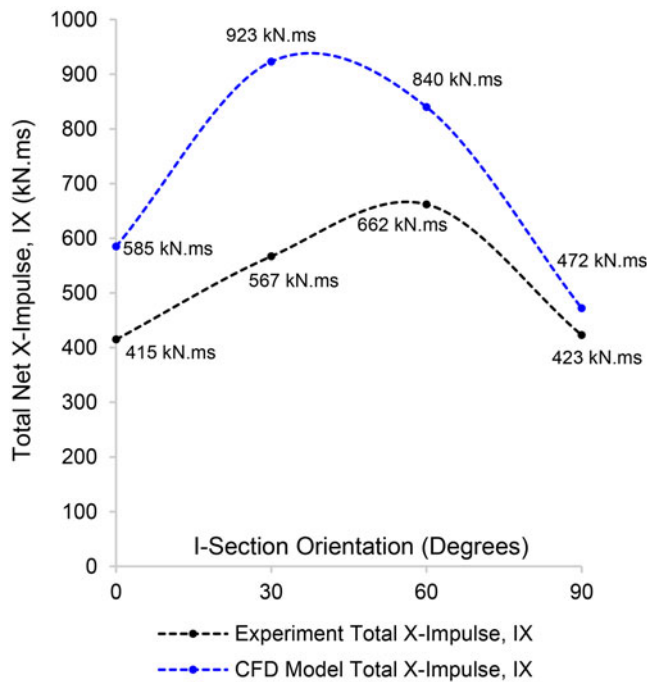


Figure 17. Net X-impulse variation with I-section orientation.

Table 7. Total net X-impulse throughout positive phase duration: experimental results vs. CFD models.

	Total net X-impulse during positive phase duration, I_x (kN.ms)			
	0°	30°	60°	90°
Experiment	415	567	662	423
CFD Model	585	923	840	472
% Error	40.9%	62.3%	26.9%	11.6%

Results of numerical models were compared to new experimental measurements to assess the predictive capacity of inviscid Eulerian CFD as a tool for calculating long-duration blast drag loading on intricate cross-sectional geometries.

Numerical incident blast waves demonstrated good agreement with experimental trials in terms of peak overpressure, positive phase duration and total impulse. CFD models calculated blast pressures with good experimental agreement for geometric surfaces directly exposed to the shockwave, demonstrating good predictive capacity towards calculating stagnation pressure–time histories on exposed finite geometry surfaces. CFD models generally underestimated stagnation pressures and impulses on shielded, rear-facing geometry surfaces despite the numerical incident blast wave exhibiting good agreement to the experimental environment. Reduced agreement occurred at oblique, bluff I-section orientations where shielded surfaces were susceptible to complex aerodynamic processes such as flow separation, low-pressure wake regions and vorticity. These discrepancies were attributed to unresolvable aerodynamic processes limited by the inviscid Eulerian solver and absence of a numerical turbulence model. Underestimation of stagnation pressures on rear-facing, shielded geometry surfaces manifested as overestimated resultant loading, notably exceeding experimental results. Resultant blast loading was most significantly overestimated by analyses at bluff, oblique I-

section orientations where complex aerodynamic effects were predominant.

Importantly, this study provides new awareness of the capability and limitations of inviscid hydrocodes for long-duration blast loads on finite geometries where drag loading is predominant. Improved accuracy of numerical blast loading analyses may be addressed by employing viscous Navier–Stokes solvers and turbulence models capable of resolving complex aerodynamic flow and boundary layer effects. No analysis platforms with shock wave modelling capabilities are openly available at present that can practically or reliably resolve these complex effects, particularly at the large spatial and temporal scales inherent to long-duration blasts. Increasingly sophisticated models will naturally require further computational expense and resource, which may not be practical for modelling long-duration blast problems. Results of this study indicate that Eulerian CFD analyses tend to overpredict net loading on finite geometries when long-duration blast interaction and resulting drag loading is of concern. When used as the basis for structural response calculations, this study suggests that Eulerian CFD analyses provide conservative loading calculations, although reduced accuracy can be expected where complex aerodynamic processes have significant influence.

Acknowledgements

The authors would like to express their gratitude to the UK Ministry of Defence for allowing use of the blast testing facilities at MOD Shoeburyness. All data obtained while using these facilities remain the property of the UK MOD. The assistance of the Spurpark Ltd. trials division during preparation and interpretation of experimental trials is gratefully acknowledged.

Disclosure statement

No potential conflict of interest was reported by the authors.

Funding

The authors wish to thank the UK EPSRC and AWE plc for financial support.

ORCID

Jack W. Denny  <http://orcid.org/0000-0003-3835-9169>

References

- Anderson, J. D. J. (2009). *Computational fluid dynamics—An introduction*. Berlin: Springer.
- Atkinson, G., & Cusco, L. (2011). Buncefield: A violent, episodic vapour cloud explosion. *Process Safety and Environmental Protection*, 89(6), 360–370. doi:10.1016/j.psep.2011.06.019
- Ballantyne, G., Whittaker, A. S., Aref, A. J., & Dargush, G. F. (2009). *Air blast effects on structural shapes*. Technical Report MCEER-09-0002.
- Ballantyne, G. J., Whittaker, A. S., Dargush, G. F., & Aref, A. J. (2010). Air-Blast effects on structural shapes of finite width. *Journal of Structural Engineering*, 136(2), 152–159. doi:10.1061/(ASCE)ST.1943-541X.0000049

- Bogosian, D., Ferritto, J., & Shi, Y. (2002). Measuring uncertainty and conservatism in simplified blast models. In 30th Explosives Safety Seminar, Atlanta, GA, pp. 1–26.
- Borvik, T., Hanssen, A. G., Langseth, M., & Olovsson, L. (2009). Response of structures to planar blast loads—A finite element engineering approach. *Computers and Structures*, 87(9–10), 507–520. doi:10.1016/j.compstruc.2009.02.005
- Century Dynamics (2011). *AUTODYN theory manual*. Horsham: Century Dynamics Inc.
- Chapman, T. C., Rose, T. A., & Smith, P. D. (1995). Blast wave simulation using AUTODYN2D: A parametric study. *International Journal of Impact Engineering*, 16(5–6), 777–787. doi:10.1016/0734-743X(95)00012-Y
- Clough, L. (2016). Synergistic response of steel structures to thermal and blast loading. University of Southampton, UK.
- Clubley, S. K. (2014). Non-linear long duration blast loading of cylindrical shell structures. *Engineering Structures*, 59, 113–126. doi:10.1016/j.engstruct.2013.10.030
- Craft, T. J. (2010). *Inviscid flows—Fluid mechanics*. University of Manchester, UK.
- Denny, J. W. (2017). Investigating multi-axis long-duration blast response of steel column sections. University of Southampton, UK.
- Denny, J. W., & Clubley, S. K. (2019). Long-duration blast loading & response of steel column sections at different angles of incidence. *Engineering Structures*, 178, 331–342. doi:10.1016/j.engstruct.2018.10.019
- Fairlie, G. E. (1998). *The numerical simulation of high explosives using AUTODYN-2D & 3D*. In *Explo '98*, Institute of Explosive Engineers 4th Biannual Symposium.
- Johns, R. V., & Clubley, S. K. (2016). The influence of structural arrangement of long-duration blast response of annealed glazing. *International Journal of Solids and Structures*, 97–98, 370–388. doi:10.1016/j.ijsolstr.2016.07.012
- Kingery, C. N., & Bulmash, G. (1984). *Airblast parameters from tnt spherical air burst and hemispherical surface burst*. Technical Report ARBRL-TR-02555.
- Krauthammer, T. (2008). *Modern protective structures*. Boca Raton, FL: CRC Press.
- Lee, E. L., Hornig, H. C., & Kury, J. W. (1968). *Adiabatic expansion of high explosive detonation products*. Report UCRL-50422.
- Mays, G., & Smith, P. (1995). *Blast effects on buildings*. London: Thomas Telford.
- Remennikov, A. M., & Rose, T. A. (2005). Modelling blast loads on buildings in complex city geometries. *Computers & Structures*, 83(27), 2197–2205. doi:10.1016/j.compstruc.2005.04.003
- Rigby, S. E., Tyas, A., Bennett, T., Stephen, D., Clarke, S. D., Warren, J. A., ... Warren, J. A. (2014). A numerical investigation of blast loading and clearing on small targets. *International Journal of Protective Structures*, 5(3), 253–274
- Rose, T. A. (2006). *Air3D Version 9.0—Computational tool for airblast calculations*. Engineering Systems Department, Cranfield University.
- Schraml, S. J., & Hisley, D. M. (1995). *Euler and Navier-Stokes simulations of shock wave interaction with a generic block target*. ARL-TR-848.
- Sherkar, P., Whittaker, A. S., & Aref, A. J. (2010). *Modeling the effects of detonations of high explosives to inform blast-resistant design*. Technical Report MCEER-10-0009.
- Shi, Y., Hao, H., & Li, Z.-X. (2007). Numerical simulation of blast wave interaction with structure columns. *Shock Waves*, 17(1–2), 113–133. doi:10.1007/s00193-007-0099-5
- Smith, P. D., & Hetherington, J. G. (1994). *Blast and ballistic loading of structures*. Boca Raton, FL: CRC Press.
- Steel Construction Institute (2009). *Buncefield explosion mechanism phase 1 (Volumes 1 and 2)*. Health and Safety Executive, Ascot.
- Tabatabaei, Z. S., Volz, J. S., Baird, J., Gliha, B. P., & Keener, D. I. (2013). Experimental and numerical analyses of long carbon fiber reinforced concrete panels exposed to blast loading. *International Journal of Impact Engineering*, 57, 70–80.
- US Department of Defense (DoD) (2008). *Structures to resist the effects of accidental explosions. Unified Facilities Criteria (UFC) 3-340-02*. Washington, DC.
- U.S. Chemical Safety Board (2013). *Preliminary findings into the west fertilizer explosion and fire*.